Unravelling the Electronic Structure and Dynamics of the Atomically Dispersed Iron Sites in Electrochemical CO_2 Reduction

Yaqiong Zeng[a,b], Jian Zhao[a], Shifu Wang[a,c], Xinyi Ren[a,b], Yuanlong Tan[a], Ying-Rui Lu[d], Shibo Xi[e], Junhu Wang[f], Frédéric Jaouen[g,*], Xuning Li[a,*], Yanqiang Huang[a], Tao Zhang[a], and Bin Liu[h,*]

[a]*State Key Laboratory of Catalysis, Dalian Institute of Chemical Physics, Chinese Academy of Sciences, Dalian 116023, P.R. China.*

[b]*University of Chinese Academy of Sciences, Beijing 100049, P.R. China.*

[c]*Department of Chemical Physics, University of Science and Technology of China, Hefei 230026, P.R. China.*

[d]*National Synchrotron Radiation Research Center, Hsinchu 300, Taiwan.*

[e]*Institute of Chemical and Engineering Sciences, A*STAR, Singapore 627833, Singapore.*

[f]*Center for Advanced Mössbauer Spectroscopy, Mössbauer Effect Data Center, Dalian Institute of Chemical Physics, Chinese Academy of Sciences, Dalian 116023, P. R. China.*

[g]*Institut Charles Gerhardt Montpellier, CNRS, Université de Montpellier, ENSCM, 34293 Montpellier, France.*

[h]*School of Chemical and Biomedical Engineering, Nanyang Technological University, 62 Nanyang Drive, Singapore 637459, Singapore.*

*Corresponding Authors:

frederic.jaouen@umontpellier.fr (F.J.)

lixn@dicp.ac.cn (X.L.)

liubin@ntu.edu.sg (B.L.)

Graphical abstract

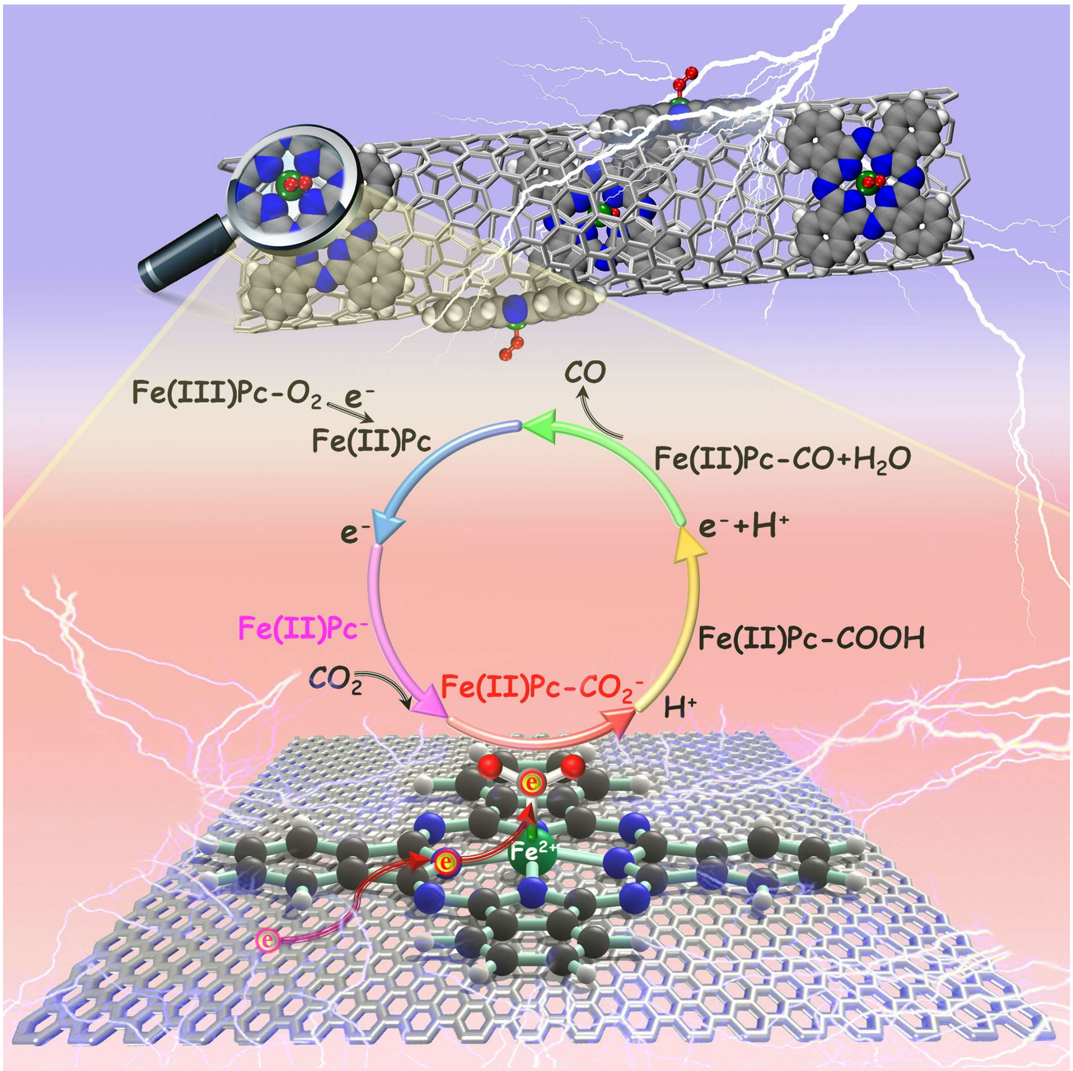

Abstract

Single-atom catalysts with a well-defined metal center open unique opportunities for exploring the catalytically active site and reaction mechanism of chemical reactions. However, understanding of the electronic and structural dynamics of single-atom catalytic centers under reaction condition is still limited due to the challenge of combining *operando* techniques that are sensitive to such sites and model single-atom systems. Herein, supported by state-of-the-art *operando* techniques, we provide an in-depth study of the dynamic structural and electronic evolution during electrochemical CO_2 reduction reaction (CO_2RR) of a model catalyst comprising iron only as a high-spin (HS) Fe(III)N_4 center in its resting state. *Operando* ^{57}Fe Mössbauer and X-ray absorption spectroscopies clearly evidence the change from a HS Fe(III)N_4 to a HS Fe(II)N_4 center with decreasing potential, CO_2- or Ar-saturation of the electrolyte leading to different adsorbates and stability of the HS Fe(II)N_4 center. With *operando* Raman spectroscopy and cyclic voltammetry, we identify that the phthalocyanine (Pc) ligand coordinating the iron cation center undergoes a redox process from Fe(II)Pc to Fe(II)Pc^-. Altogether, the HS Fe(II)Pc^- species is identified as the catalytic intermediate for CO_2RR. Furthermore, theoretical calculations reveal that the electroreduction of the Pc ligand modifies the d-band center of the *in situ* generated HS Fe(II)Pc^- species, resulting in an optimal binding strength to CO_2 and thus boosting the catalytic performance of CO_2RR. This work provides both experimental and theoretical evidence towards the electronic structural and dynamics of reactive sites in single-Fe-atom materials and shall guide the design of novel efficient catalysts for CO_2RR.

Introduction

Revealing the nature of active sites in heterogeneous metal-based catalysts is essential for the fine control of the reaction kinetics and dynamics [1-3]. However, the geometric and electronic structures of active sites are usually influenced by many parameters such as the nature of the metal atoms[4,5], the nature of coordinating atoms (C, N, O, S, *etc.*)[6], coordination numbers[7], secondary coordination spheres[8,9], *etc*., which leads to great challenges in identifying structure-activity relationships and the underlying reaction mechanisms[10,11]. Moreover, due to the dynamic behaviors of active sites during catalysis and the issues of current characterization techniques, the atomic-level understanding of the active sites during a chemical reaction remains challenging[12-15].

Single-atom catalysts (SACs) with well-defined and atomically-dispersed metal sites are a promising platform for the precise identification of structure-activity relationships and, on the practical level, for the full utilization of the metal[16-20]. Recent studies highlighted that single-atom active sites can undergo dynamic evolution under reaction conditions, induced by applied temperature, electrochemical potential, adsorbates, and *etc*., challenging the identification of the true structure of the catalytic site, and of structure-catalysis relationships[21-24]. Therefore, real-time monitoring the structural evolution of active sites in SACs under realistic operating conditions is highly desired.

The development of *in situ/operando* techniques and setups such as X-ray absorption spectroscopy (XAS), Fourier transform infrared spectroscopy (FT-IR), Raman spectroscopy, *etc.* for probing SACs offers new opportunities for identifying the active sites, capturing the reaction intermediates, and uncovering the catalytic mechanism[25,26]. For instance, relying on *operando* XAS, Hu's group showed with *operando* Fe K-edge XAS the high activity, selectivity and stability of Fe(III) sites in a Fe-N-C SAC for CO_2RR to CO[27]. The iron was shown to remain in +3 oxidation state down to -0.4 V vs. RHE, while at -0.5 V vs. RHE, its oxidation state decreased to +2 but the CO_2RR activity concomitantly became unstable and lower. The maintained ferric oxidation state down to -0.4 V vs. RHE in this Fe-N-C material prepared by pyrolysis at 900 °C of Fe-doped ZIF-8 was assigned to a pyrrolic nitrogen environment, and an analogy made to the similarly low Fe(III)/Fe(II) redox potential of some iron porphyrins. In contrast, Li *et al.* concluded that H_2O-Fe(II)N_4 is the most active site for selective CO_2RR to CO for a Fe-N-C SAC material derived from the flash pyrolysis at 1050 °C of Fe acetate and ZIF-8, on the basis of *operando* Fe K-edge XAS results and theoretical calculations[28]. It is of note that the Zn content in ZIF-8 derived Fe-N-C materials is much higher after pyrolysis at 900 °C than at 1050 °C (Zn boiling point 907 °C), which could play a role on the carbon structure and, indirectly, on the detailed structure and reactivity of FeN_xC_y moieties sites. Recently, we studied another Fe-N-C catalyst derived from ZIF-8 via pyrolysis. Taking advantage of *operando* ^{57}Fe Mössbauer spectroscopy, we unveiled the *in situ* generation of the low-spin monovalent Fe(I) site at -0.9 V vs. RHE, and assigned it as the most reactive center in CO_2RR[29]. The contrasting and apparently inconsistent results from these works highlight the complexity of the real structure of catalytic sites under reaction conditions.

While the pyrolytic preparation of Fe-N-C catalysts comprising only single-metal atom sites is now relatively well-established, such materials typically feature FeN_xC_y moieties with different structures and/or electronic states (Supplementary Fig. 1), as evidenced with *ex situ* and/or *operando* spectroscopic techniques[14,27-30]. In addition, the electrochemical utilization of FeN_4 sites is usually low in pyrolyzed materials, according to either CO cryo chemisorption or nitrite stripping techniques applied for counting the active sites[31]. Only in the case of the recent CVD preparation of a Fe-N-C, was a full utilization of FeN_4 sites achieved, featuring a single HS Fe(III)N_4 site structure, as revealed by *ex situ* ^{57}Fe Mössbauer spectroscopy[32]. The low utilization of FeN_4 sites implies that *operando* spectroscopic changes are only partly related to surface sites, complexifying the analysis of the *operando* structure of active surface sites. More research efforts are therefore required towards the development of model Fe-based catalytic systems featuring a mono-structure and high electrochemical accessibility of the single-metal-atom sites, and the application on such model catalysts of *operando* characterization techniques with atomic scale sensitivity[33,34].

In this work, leaning on the long-demonstrated CO_2RR activity of metal-phthalocyanines in general[35-37], and Fe-phthalocyanines in particular[38,39], we rationally designed a model single-Fe-atom catalyst by firstly synthesizing a well-defined FePc molecule ($C_{32}H_{16}FeN_8$, with or without ^{57}Fe enriched) comprising of identical HS Fe(III) species, followed by immobilizing it on conductive carbon nanotubes. *Operando* ^{57}Fe Mössbauer, XAS, and Raman studies were conducted to investigate the dynamic evolution of the single-Fe-atom centers during electrochemical CO_2RR, revealing that the initial HS O_2-Fe(III)Pc species is irreversibly reduced to metallic iron in Ar-saturated environment, while *in-situ* generating the HS Fe(II)Pc^- active site in CO_2-saturated condition. The one-electron reduction of the Pc ligand stabilizes the Fe(II) species which, combined with the presence of the carbonate anion adsorption intermediate (Fe(II)Pc-CO_2^-), prevents the over-reduction to Fe(I) and metallic iron. Density functional theory (DFT) calculations further revealed that the *in-situ* generated HS Fe(II)Pc^- species with modified d-band center could result in an optimal binding to CO_2 molecules, promoting the CO_2RR.

Results and Discussion

Structural Characterization

The single-Fe-atom catalyst with well-defined N-coordination structure for CO_2RR was built by immobilizing the FePc molecule on conductive carbon nanotubes (CNT) via π-π interaction

(Supplementary Fig. 2)[24,40]. Fourier-transform infrared (FT-IR) spectroscopy was used to confirm the skeleton information of the as-synthesized FePc molecule. As shown in Supplementary Fig. 3, the main peaks located at 727, 1080 and 1117 cm^{-1} can be assigned to out-of- and in-plane C-H bond vibrations from the Pc ring respectively, while the bands at 1162 and 1331 cm^{-1} can be assigned to C-N and C-C stretching vibration from the isoindole structure[41-43]. The XRD pattern of the as-prepared FePc-CNT catalyst shows the characteristic peaks of both CNT and FePc, which verifies the successful loading of FePc on CNT (Supplementary Fig. 4)[44]. Furthermore, FePc uniformally covers the CNT surface, as revealed by scanning electron microscopy (SEM), transmission electron microscopy (HR-TEM) and EDX elemental mappings (Fig. 1b,c and Supplementary Fig. 5a). Meanwhile, the scanning transmission electron microscopy (STEM) and the corresponding elemental mapping images reveal the atomically dispersed Fe elements that are uniformly distributed on the entire CNT (Fig. 1c). As shown in Fig. 1d,e, the high density of bright spots in the aberration-corrected high-angle annular dark-field scanning transmission electron microscopy (HAADF-STEM) images confirm the atomically dispersed Fe species in FePc-CNT. FePc-CNT exhibits extremely similar electronic structure and environmental characteristics to pure FePc (Supplementary Fig. 6-8). The experimental X-ray absorption near edge structures (XANES) spectrum shows that the edge energy of FePc-CNT is close to that of commercial O_2-Fe(III)Pc (O_2-Fe(III)Pc-c) (Fig. 1f), supporting the ferric state and, the pre-edge peak at 7114.3 eV can be assigned to a dipole forbidden 1s→3d transition, suggesting a deviation from the FeN_4 structure due to the axial coordination of Fe cation by O_2. This can be further confirmed by the simulation of XANES spectrum using the finite difference method near-edge structure (FDMNES) calculation based on the model structure of O_2-FeN_4 (Supplementary Fig. 9). Fig. 1g shows the Fourier transformed extended X-ray absorption fine structure (FT-EXAFS) spectra of FePc-

CNT and the spectra of reference compounds. The main peak at 1.62 Å (distance not corrected for phase shift) can be assigned to the Fe-N in the first coordination shell, and is in line with the Fe-N bond distance in iron phthalocyanine, further indicating atomic dispersion of Fe species on the CNT surface. As shown in Fig. 1h, the FT-EXAFS spectrum of FePc-CNT can be well fitted using the structural model of O_2-FeN_4 (optimized by DFT), with O_2 adsorbed on Fe in end-on mode. The fitted structural parameters for FePc-CNT are listed in Supplementary Table 1. The electronic state of Fe species in the as-prepared FePc-CNT was further determined by room-temperature ^{57}Fe Mössbauer spectroscopy. As shown in Fig. 1i, the Mössbauer spectrum of FePc-CNT can be well fitted using one quadrupole doublet with an isomer shift (IS) of *ca* 0.35 mm s^{-1} and a quadrupole splitting (QS) of *ca* 0.71 mm s^{-1}, which can generally (based in particular on the low QS value), but not unambiguously, be assigned to a high spin (HS) Fe(III) species. The fitted parameters of the Mössbauer spectrum of FePc-CNT are shown in Supplementary Table 2. In the class of iron phthalocyanine materials, a HS ferric phthalocyanine was synthesized and studied by Mössbauer spectroscopy by Burtsev *et al*., with reported IS and QS values of 0.3 and 0.7 mm s^{-1} respectively, at room temperature[45]. These values match well with those observed in the present work, and, combined with the other results, support the successful synthesis of FePc-CNT with atomically dispersed HS O_2-Fe(III)N_4 species in *ex situ* conditions.

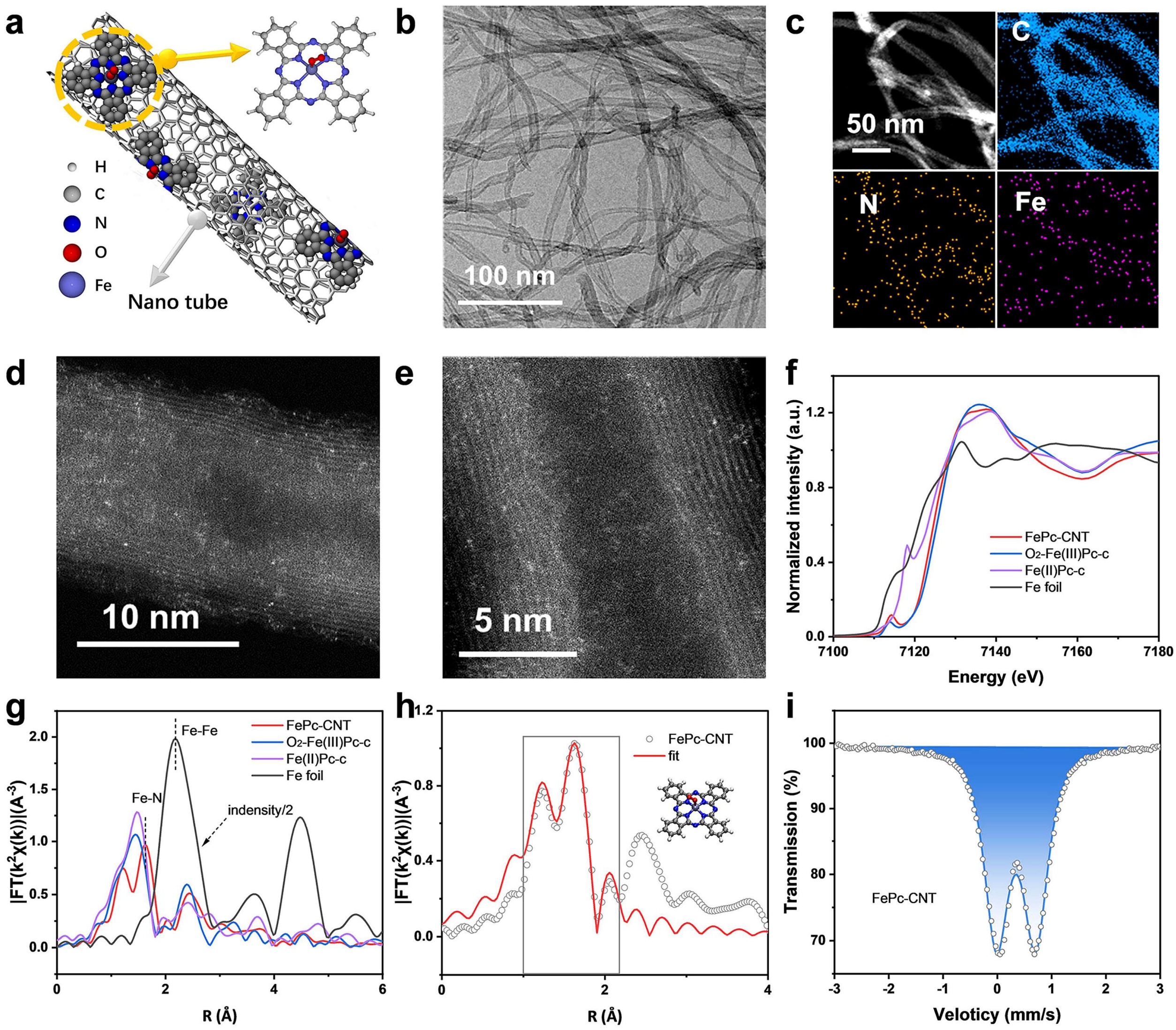

Fig. 1 | Structural characterization of the as-prepared FePc-CNT. a, Synthesis strategy of the model FePc-CNT catalyst. **b,** TEM image (scale bar, 100 nm), and **c,** energy dispersive X-ray spectroscopy (EDX) mappings for FePc-CNT (scale bar, 50 nm). **d, e,** HAADF-STEM images of FePc-CNT. **f,** Normalized Fe K-edge XANES spectrum and **g,** k^2-weighted FT-EXAFS spectrum of FePc-CNT together with those of commercial O_2-Fe(III)Pc (O_2-Fe(III)Pc-c), commercial Fe(II)Pc (Fe(II)Pc-c) and Fe foil standards for comparison. **h,** Experimental and fitted EXAFS spectrum in R-space for FePc-CNT catalyst (R range, 1-2.2 Å). **i,** Room-temperature ^{57}Fe Mössbauer spectrum of FePc-CNT.

Electrochemical performance

The electrochemical CO_2RR performance was first evaluated by linear scan voltammetry (LSV) in 0.5 M $KHCO_3$ electrolyte. As shown in Fig. 2a, a significantly higher current density is observed with FePc-CNT at *ca* -0.3 V vs. RHE in CO_2-saturated condition than in Ar-saturated condition, assigned to CO_2RR. The current density is also much larger and at much higher potential for FePc-CNT vs H_2Pc-CNT, indicating the critical role of Fe in catalysis (Fig. 2a). Cyclic voltammetry (CV) curves of FePc-CNT and H_2Pc-CNT in Ar-saturated electrolyte were recorded to explore the redox process of the catalysts. As shown in Fig. 2b, FePc-CNT features two redox peaks, and the reduction peak positions are at around +0.34 and -0.36 V vs. RHE, whereas no redox peak over H_2Pc-CNT can be observed within the -0.5 to +0.9 V vs. RHE potential window. The highest redox was assigned to Fe(III)Pc/Fe(II)Pc transition, while the low redox might be attributed to the $Fe(II)Pc/Fe(II)Pc^-$ transition[46]. Electrochemical CO_2RR activities and selectivities of FePc-CNT, H_2Pc-CNT were further evaluated in an H-cell. H_2 and CO were the only detected gas-phase products, and no liquid products were detected (Supplementary Fig. 10). As shown in Fig. 2c, the Faradaic efficiency of CO (FE_{CO}) over FePc-CNT reaches a maximum value of ~92% at -0.45 V vs. RHE, which is much higher than that over H_2Pc-CNT (~31% at -0.45 V vs. RHE). Within the whole range of potential, the bare CNT displays a H_2 favorable reaction pathway (Supplementary Fig. 11). The CO partial current density (j_{CO}) further proves the higher activity of FePc-CNT in CO_2RR compared to H_2Pc-CNT (Fig. 2d, red and black curves). By depositing FePc-CNT on a gas diffusion electrode (GDE), the CO_2RR performance of FePc-CNT was further evaluated in a flow-cell. At -0.45 V vs. RHE, j_{CO} reaches 23 mA cm^{-2} (Fig. 2d, blue curve) with FE_{CO} of ~97%. The Tafel slope of FePc-CNT of 79 mV dec^{-1} supports that the rate determining step of CO_2 to CO electroreduction is the first proton transfer (Supplementary Fig.

12). Besides initial activity and selectivity, the FE_{CO} after 10 h of continuous CO_2RR at -0.45 V vs. RHE remained higher than 88%, while the current density decreased by only 8.5%, indicating good catalytic stability of FePc-CNT towards CO_2RR (Supplementary Fig. 13).

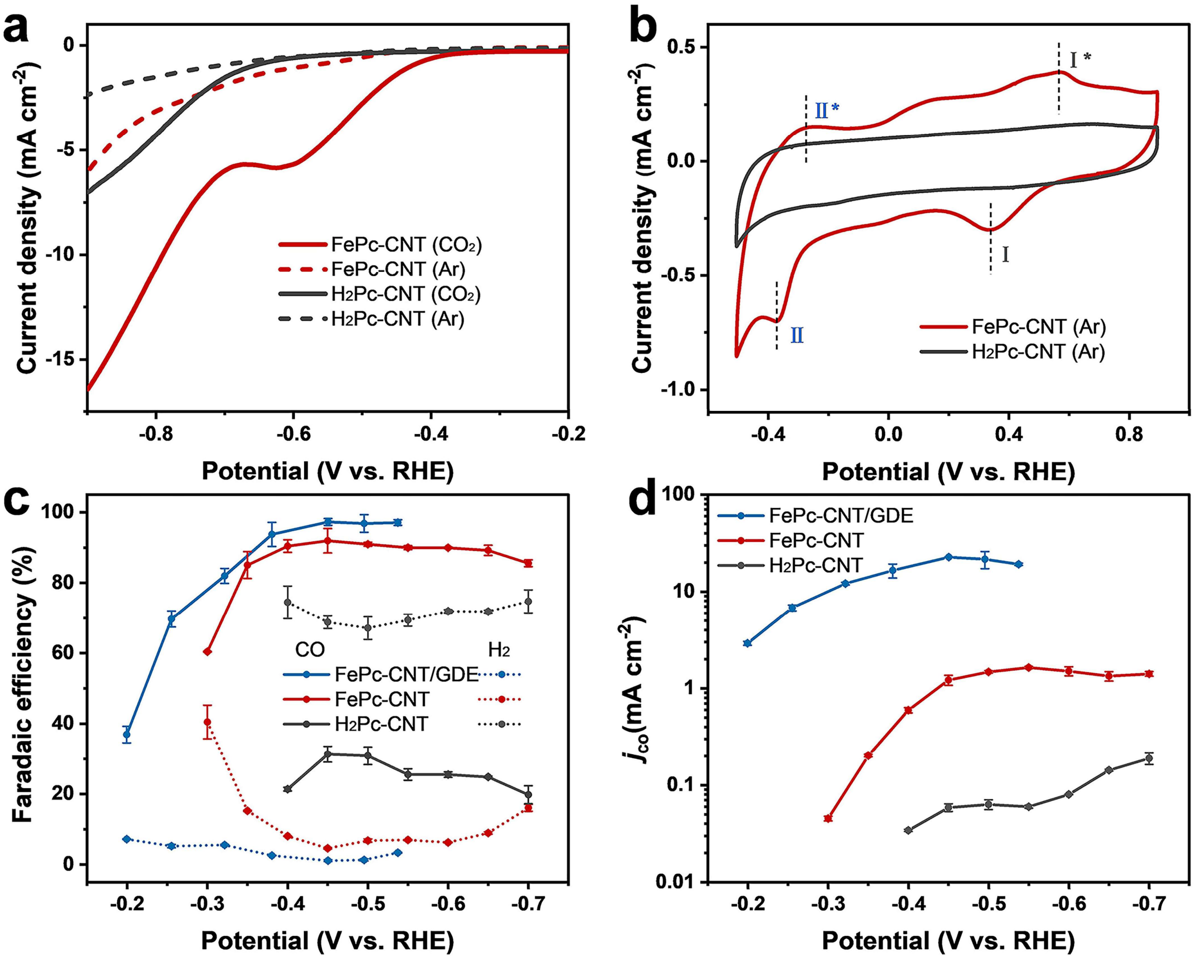

Fig. 2 | Electrochemical CO_2RR. a, Linear sweep voltammogram (LSV) curves recorded over FePc-CNT and H_2Pc-CNT at a sweep rate of 10 mV s^{-1} under Ar- and CO_2-saturated 0.5 M $KHCO_3$ electrolytes. **b,** Cyclic voltammogram (CV) curves for FePc-CNT and H_2Pc-CNT recorded in an Ar-saturated 0.5 M $KHCO_3$ electrolyte at 50 mV s^{-1}. **c,** Faradaic efficiency of CO and H_2 and **d,** Current density of CO for FePc-CNT in an H-cell (red) and on a GDE (blue) and H_2Pc-CNT in an H-cell (black).

Operando X-ray absorption spectroscopy

Operando XAS measurements were performed to reveal the evolution of the electronic structure and coordination environment of the single-Fe-atom species in FePc-CNT during the CO_2RR process. As shown in Fig. 3a, the oxidation state of Fe is higher in CO_2-saturated condition than that in Ar-saturated condition at open circuit potential (OCP), which is possibly due to a spontaneous charge transfer from the central Fe to the adsorbed CO_2 molecule. When a potential of -0.4 V vs. RHE was applied, the Fe K-edge of FePc-CNT shifted to lower energies, in both Ar- and CO_2-saturated 0.5 M $KHCO_3$ solution (Fig. 3a). As the applied potential decreased, the central iron of FePc-CNT was gradually reduced from Fe(III) into Fe(II). When the electrochemical potential was removed, the XANES spectrum of FePc-CNT was slightly different compared to the initial OCP condition (Fig. 3b), for measurements in CO_2 saturated electrolyte. This indicates that the Fe(III) to Fe(II) reduction is not completely reversible, possibly as a result of a change in the axial ligand present atop Fe before and after CO_2RR (Fig. 3b). The evolution of the pre-edge region in the *operando* Fe K-edge XANES spectra further reveals the structural dynamics of single-Fe-atom species. As shown in Fig. 3c, under OCP condition, the pre-edge exhibits identical feature of O_2-Fe(III)N_4 (pre-edge peak B)[47]. At -0.4 V vs. RHE, the intensity of the pre-edge peak B decreased, while a new pre-edge peak C appeared at 7118.3 eV. The latter is ascribable to $1s \rightarrow 4p_z$ transition and can be indexed to square planar D_{4h} symmetric structure of Fe(II)Pc, indicating the structural switching from non-planar to planar structure when the axial ligand is removed. With further decreasing the potential to -0.8 V vs. RHE, a non-negligible pre-edge peak (A) at the lower energy of 7112.5 eV was observed, which can be assigned to a distorted square planar structure with axial ligand[48,49]. The peak A is more intense at -0.8 than at -0.4 V vs. RHE, and disappears after removing the potential (labelled as AFT in the figure), suggesting that the peak A is most likely related to a catalytic intermediate. To determine the exact structure of the catalytic intermediate, we used the FDMNES calculation method to simulate the XANES spectra obtained at OCP and -0.8 V vs. RHE. The geometric configuration and atom coordinates for the calculated models are shown in Supplementary Fig. 14 and Supplementary Table 3-5. As shown in Fig. 3d and Supplementary Fig. 15-17, the pre-edge peaks A, B, and C match well with the structure model of Fe(II)Pc-CO_2^-, O_2-Fe(III)Pc, and Fe(II)Pc, respectively. These assignments are also in line with the fact that the redox wave for the Pc ligand reduction to Pc^- in Fe(II)Pc-CNT is situated at *ca* -0.4 V vs. RHE (Fig. 2b), and could explain the enhanced adsorption of CO_2 on Fe(II)Pc^- at -0.8 V vs. RHE. All of the above results clearly show the transformation of O_2-Fe(III)Pc to Fe(II)Pc and the *in situ* formation of Fe(II)Pc-CO_2^- species as a key catalytic intermediate during the CO_2RR.

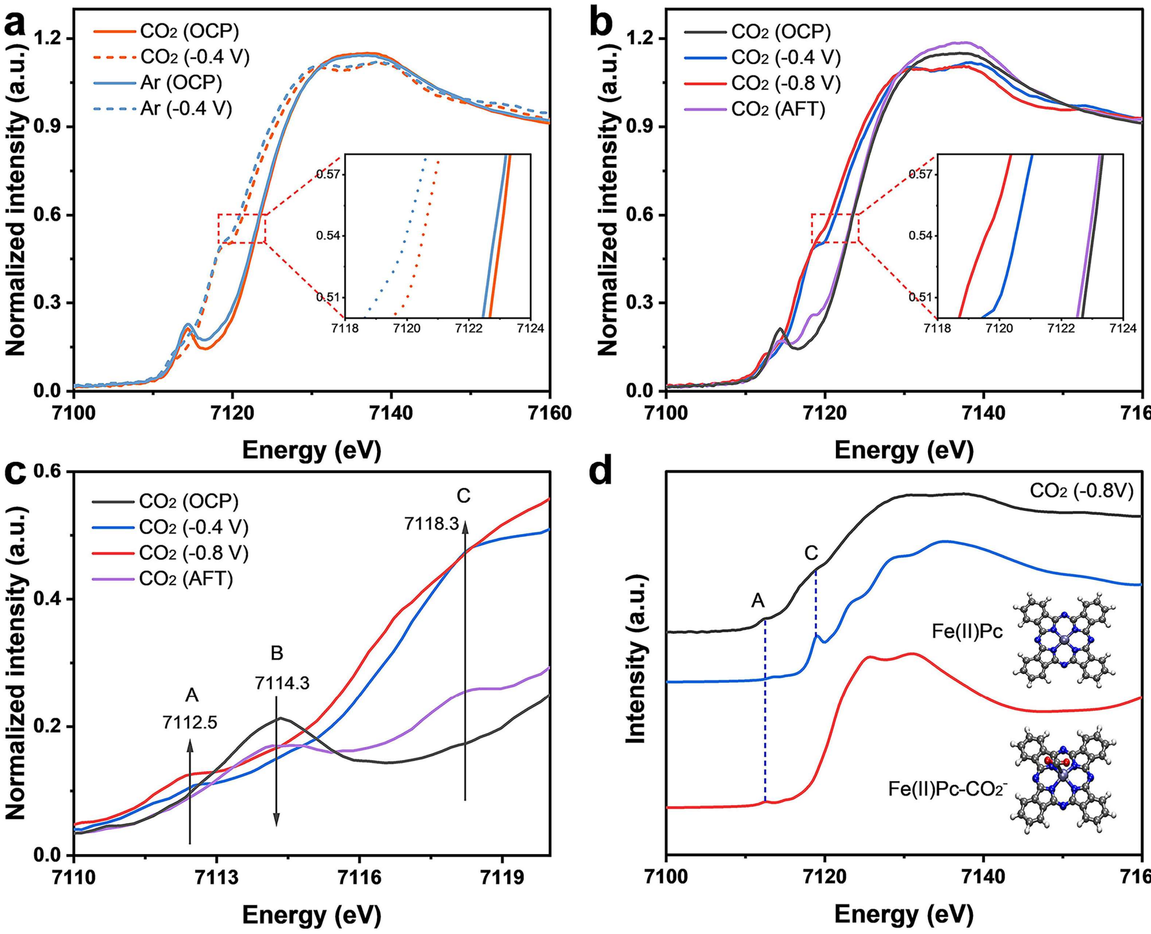

Fig. 3 | *Operando* XAS characterization. a, Normalized Fe K-edge XANES spectra of FePc-CNT, recorded at OCP and -0.4 V vs. RHE under Ar- and CO_2-saturated 0.5 M $KHCO_3$. **b,** *Operando* normalized Fe K-edge XANES spectra of FePc-CNT recorded at OCP, -0.4 V, -0.8 V vs. RHE, and AFT in CO_2-saturated 0.5 M $KHCO_3$. **c,** The magnified *operando* XANES spectra. **d,** Comparison between the experimental Fe K-edge XANES spectrum (black curve) and the theoretical spectra calculated based on Fe(II)Pc-CO_2^- (red curve) and Fe(II)Pc (blue curve).

Operando ^{57}Fe Mössbauer spectroscopy

Operando ^{57}Fe Mössbauer spectroscopy was performed to quantitatively monitor the *operando* formed catalytic intermediates in ^{57}Fe enriched FePc-CNT during CO_2RR. Fig. 4f displays the current-time curves during the *operando* Mössbauer measurements. The ^{57}Fe Mössbauer spectra acquired at different applied potentials in both CO_2- and Ar-saturated 0.5 M $KHCO_3$ solution are presented in Fig. 4a-e. The quadrupole doublet (labeled D1) with an IS value of 0.33 mm s^{-1} and a QS value of 0.69 mm s^{-1} detected at OCP is similar to the doublet observed in the *ex situ* spectrum, and can be assigned to the HS Fe(III) in O_2-Fe(III)Pc (Fig. 4a). At -0.4 V vs. RHE, two new doublets (IS = 1.19 mm s^{-1}, QS = 1.80 mm s^{-1} (D2a), and IS = 1.18 mm s^{-1}, QS = 2.50 mm s^{-1} (D2b)) are observed (Fig. 4b), both of which can be unambiguously assigned to HS Fe(II) species on the sole basis of their high IS values[50,51]. These QS values are in line with those recently experimentally reported *in situ* for HS Fe(II)N_4 sites (with IS values > 0.7 mm s^{-1} in all cases) of pyrolyzed Fe-N-C catalysts developed for oxygen electroreduction reaction[14], (QS of *ca* 2.0 mm s^{-1}, measured at 0.2-0.4 V vs. RHE in O_2-free acidic electrolyte, QS of *ca* 2.41-2.46 mm s^{-1} measured at 0.5-0.7 V vs. RHE in O_2-saturated alkaline electrolyte[13], QS of *ca* 2.1 mm s^{-1} at 0.2 V vs. RHE in O_2-free acidic electrolyte[34]). The fitted parameters of the Mössbauer spectra of FePc-CNT acquired at different potentials (OCP, -0.4, -0.8 V vs. RHE, in CO_2 saturated electrolyte) in the present work are listed in Supplementary Table 6, and the corresponding spectra are shown in Fig. 4a-c. The relative signal intensity for D1 decreases with decreasing potential in CO_2 -saturated $KHCO_3$, from 100% at OCP to 20% at -0.8 V vs. RHE. The relative signal intensity for D2a is 55% at -0.4 V vs. RHE in CO_2-saturated $KHCO_3$, and almost unmodified at -0.8 V vs. RHE (53%). In contrast, the relative signal intensity for D2b is only 12% at -0.4 V vs. RHE CO_2-saturated $KHCO_3$ but increases to 26% at -0.8 V vs. RHE. These trends are visualized in Fig. 4g, and mainly indicate the reduction of HS Fe(III) to HS Fe(II) as a consequence of the applied potential, in the condition of CO_2RR. The larger QS value for D2b vs. D2a in the present work implies increased asymmetry around the central Fe sites, which may result from the *in situ* formation of an axial intermediate of FePc-CO_2^-, well consistent with the *operando* XAS results. After removing the applied potential, the relative signal intensity of D1 species increased back to 51%, the relative signal intensity for D2a remained quite unchanged (slight decrease from 53 to 49%), while the signal for D2b species disappeared (Fig. 4d and Supplementary Table 6). When comparing the Mössbauer spectra at -0.4 V vs. RHE in CO_2-saturated vs. Ar-saturated 0.5 M $KHCO_3$ solution, a sextet with hyperfine field of 324 kOe was detected (Fig. 4e), indicating the partial transformation of FeN_4 sites into metallic iron in CO_2-free electrolyte. This indicates the stabilization of Fe(II)Pc^- by a CO_2 adsorbate or by another CO_2RR intermediate. Fig. 4h summarizes the dynamic evolution of the single-Fe-atom species in FePc-CNT during catalysis in CO_2- and Ar-saturated electrolytes.

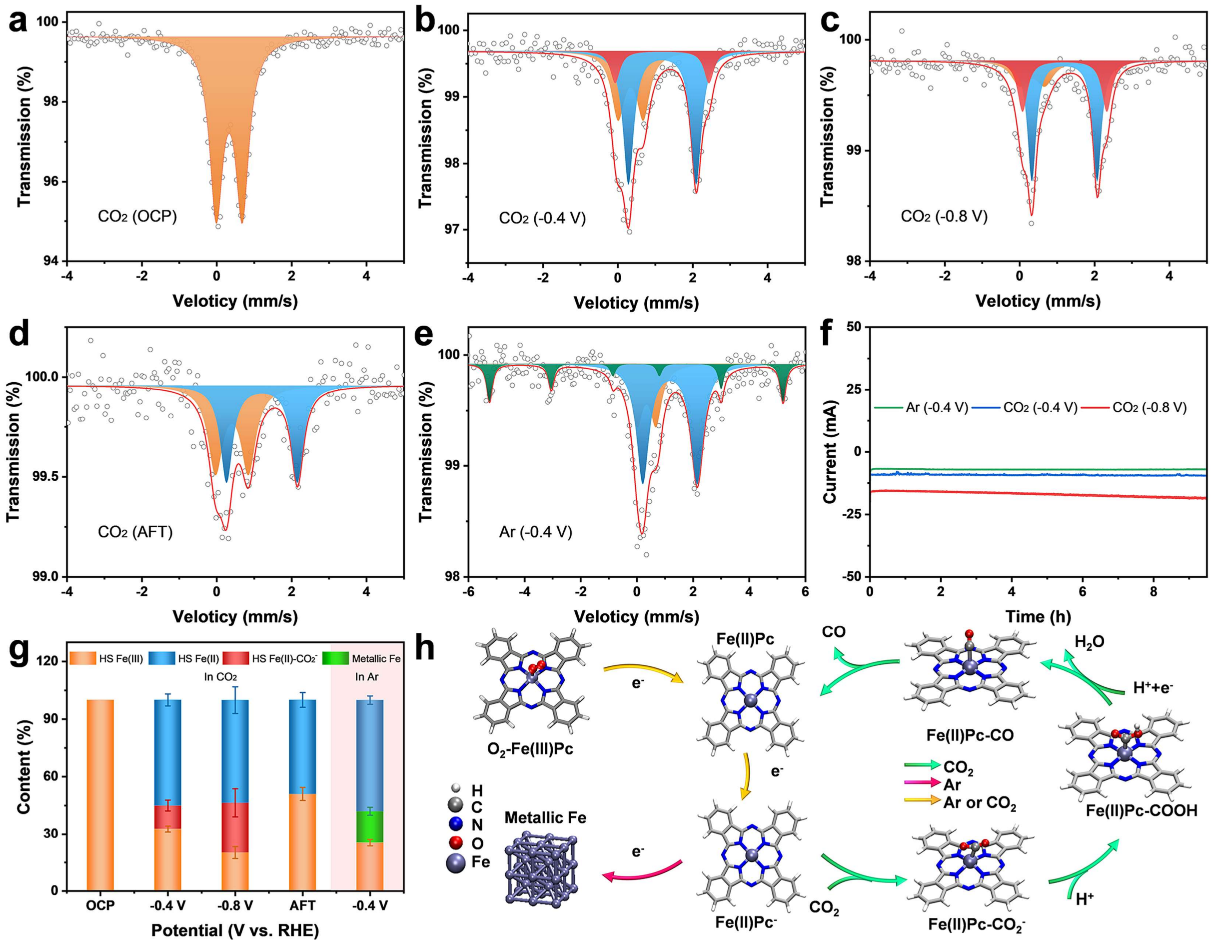

Fig. 4 | *Operando* ^{57}Fe Mössbauer characterization. *Operando* ^{57}Fe Mössbauer spectra of FePc-CNT collected at **a,** OCP, **b,** -0.4 V vs. RHE, **c,** -0.8 V vs. RHE, and **d,** AFT under CO_2-saturated 0.5 M $KHCO_3$ electrolyte. **e,** *Operando* ^{57}Fe Mössbauer spectra of FePc-CNT collected at -0.4 V vs. RHE under Ar-saturated 0.5 M $KHCO_3$ electrolyte. **f,** Current-time response of FePc-CNT in *operando* ^{57}Fe Mössbauer measurements. **g,** Relative signal intensity of different Fe species obtained from the fitting of *in situ* and/or *operando* ^{57}Fe Mössbauer measurements. **h,** The proposed dynamic evolution routes of single-Fe-atom species during catalysis under CO_2- and Ar-saturated conditions.

Operando Raman spectroscopy

To gain more insights into the role of ligands coordinated to single-Fe-atom species under reaction condition, *operando* Raman spectroscopy measurements were carried out. The Raman peak at 1532 cm^{-1} can be clearly observed over FePc-CNT at OCP under Ar-/CO_2-saturated conditions (Fig. 5a,b, Supplementary Fig. 18), which can be assigned to the C=N vibration peak [52-54]. In Supplementary Fig. 18a,b, under an Ar atmosphere, within the potential range from 0.5-0.3 V vs. RHE (covering the redox transition from Fe(III) to Fe(II) in FePc-CNT), no obvious change in the general features of the spectra was observed, indicating the lack of effect of the iron cation oxidation state on the vibrational spectra. Notably, at -0.4 V vs. RHE, which is within the second reduction region of FePc-CNT, the intensity of the C=N vibration in FePc-CNT was significantly increased (Fig. 5a), suggesting that the change of the vibration peak was derived from the reduction of the Pc ring, instead of the redox transition from Fe(II) to Fe(I)[55]. Negligible changes could be observed at -0.8 V vs. RHE and after removing the applied voltage (as compared to the case at -0.4 V vs. RHE), indicating that the Pc ring could be kept in the reduced state (Fig. 5a,b). Under CO_2-saturated condition, similar trends were obtained as compared to those in Ar-saturated condition, where the intensity of the C=N vibration peak increased when the cathodic polarization decreased to -0.4 V and -0.8 V vs. RHE (Fig. 5c,d and Supplementary Fig. 18e). Interestingly, the intensity of the peak at 750 cm^{-1} (belonging to the C–N–C bending coupled to the Fe-N stretching vibration[56,57]) dramatically decreased compared to its neighbor at 682 cm^{-1} as the electrochemical potential decreased (Fig. 5c,d), which can be ascribed to the adsorption of CO_2 molecule on the single Fe atom site with *in situ* formation of Fe(II)Pc-CO_2^- intermediate. After removing the applied potential, the intensity of the peak at 750 cm^{-1} increased back to its initial value (AFT curve in Fig. 5c). This can be explained by the loss of the intermediate species. Considering that mainly Fe(II) species and a minority Fe(III) species could be observed from *operando* Mössbauer measurements under CO_2 condition, the absence of stable Fe(I) species can be explained on the basis of the preferred one-electron reduction of the Pc ring as compared to the Fe(II) to Fe(I) reduction.

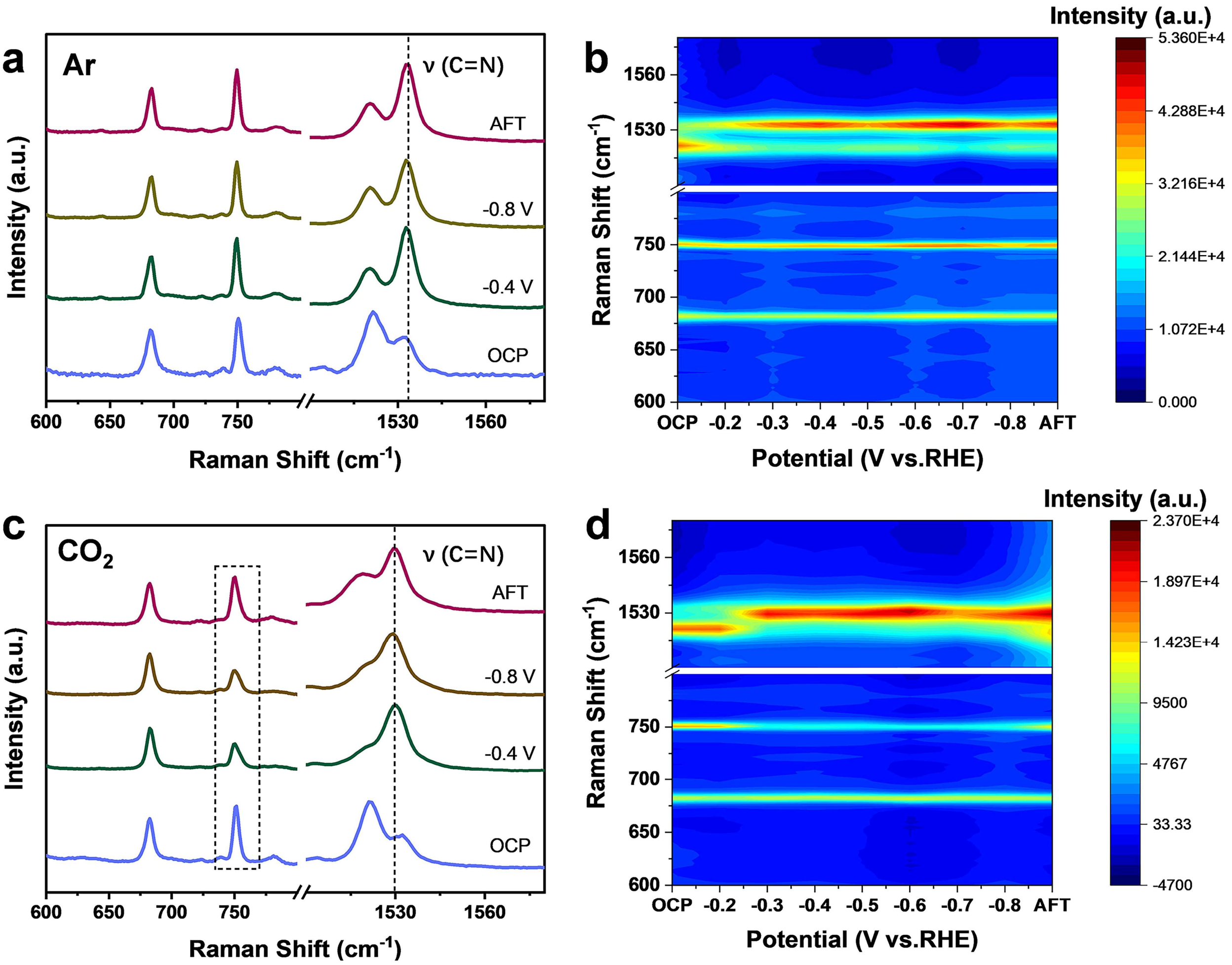

Fig. 5 | *Operando* Raman characterization. a, *Operando* Raman spectra of FePc-CNT recorded at OCP and -0.4 V, -0.8 V vs. RHE and AFT in Ar-saturated 0.5 M $KHCO_3$ solution. **b,** The corresponding contour map at full potential under Ar-saturated 0.5 M $KHCO_3$ condition. **c,** *Operando* Raman spectra of FePc-CNT recorded at OCP, -0.4 V, -0.8 V vs. RHE and AFT in CO_2-saturated 0.5 M $KHCO_3$ solution. **d,** The corresponding contour map at full potential under CO_2-saturated 0.5 M $KHCO_3$ condition.

Density functional theory calculations

DFT calculations were conducted to provide theoretical insights into the underlying reaction mechanism of electrochemical CO_2 reduction over single-Fe-atom catalyst. As shown in Supplementary Fig. 19, the single point energy of Fe(II)Pc$^-$ is much lower than that of Fe(I)Pc (ΔE =

$E_{\mathrm{Fe(I)Pc}} - E_{\mathrm{Fe(II)Pc}^-} = 0.231$ eV), confirming the preferred reduction of Pc ring with the formation of Fe(II)Pc^-. Furthermore, the delocalized electrons on the Pc ring lead to increased orbital energy levels, which can shift the d-band center of the central Fe from -4.925 eV to -4.575 eV (Fig. 6a) and decrease the CO_2 adsorption energy from -0.816 eV to -2.047 eV, resulting in the transformation of the adsorption configuration from physical adsorption to chemisorption (Fig. 6b). Obviously, the dz^2 orbital of Fe(II) was changed into a more delocalized state as the electron added to the Pc ring and thus forming of a strong covalent bond with CO_2 easily (Fig. 6c). The electronic structures of Fe(II)Pc and Fe(II)Pc^- were further investigated by charge density difference and electron spin density distribution. As shown in Supplementary Fig. 20, compared to Fe(II)Pc, a larger electronic density is delocalized at the vertical direction of Fe atom in Fe(II)Pc^-. In Fig. 6d, the electron spin density distribution of Fe(II)Pc is mainly distributed around the central Fe and the N atoms in the first coordination shell, while that of Fe(II)Pc^- is mainly distributed in the second coordination shell. Simultaneously, the electron spin density distribution of the Fe atom increases in the Z direction, which shall benefit CO_2 activation at the HS Fe(II)Pc^- site. Subsequently, the electron spin density distribution in the second coordination shell of FePc remained quite stable when bond to different intermediate species. Fig. 6e shows the energy-level correlation diagrams of Fe(II)Pc, Fe(II)Pc^-, and Fe(II)Pc-CO_2^-. It is shown that the transfer of electrons to the Pc ring with the formation of Fe(II)Pc^- pushes up the total d orbitals, especially the dz^2 orbital of Fe, which leads to a stronger charge-transfer interaction from the Fe dz^2 to CO_2 π^* orbital, accelerating the formation of Fe(II)Pc-CO_2^- intermediate and boosting the CO_2 reduction reaction. All these theoretical insights are well consistent with the results obtained from *operando* measurements, clearly illustrating the electronic structure and dynamics of the atomically dispersed iron sites in CO_2RR.

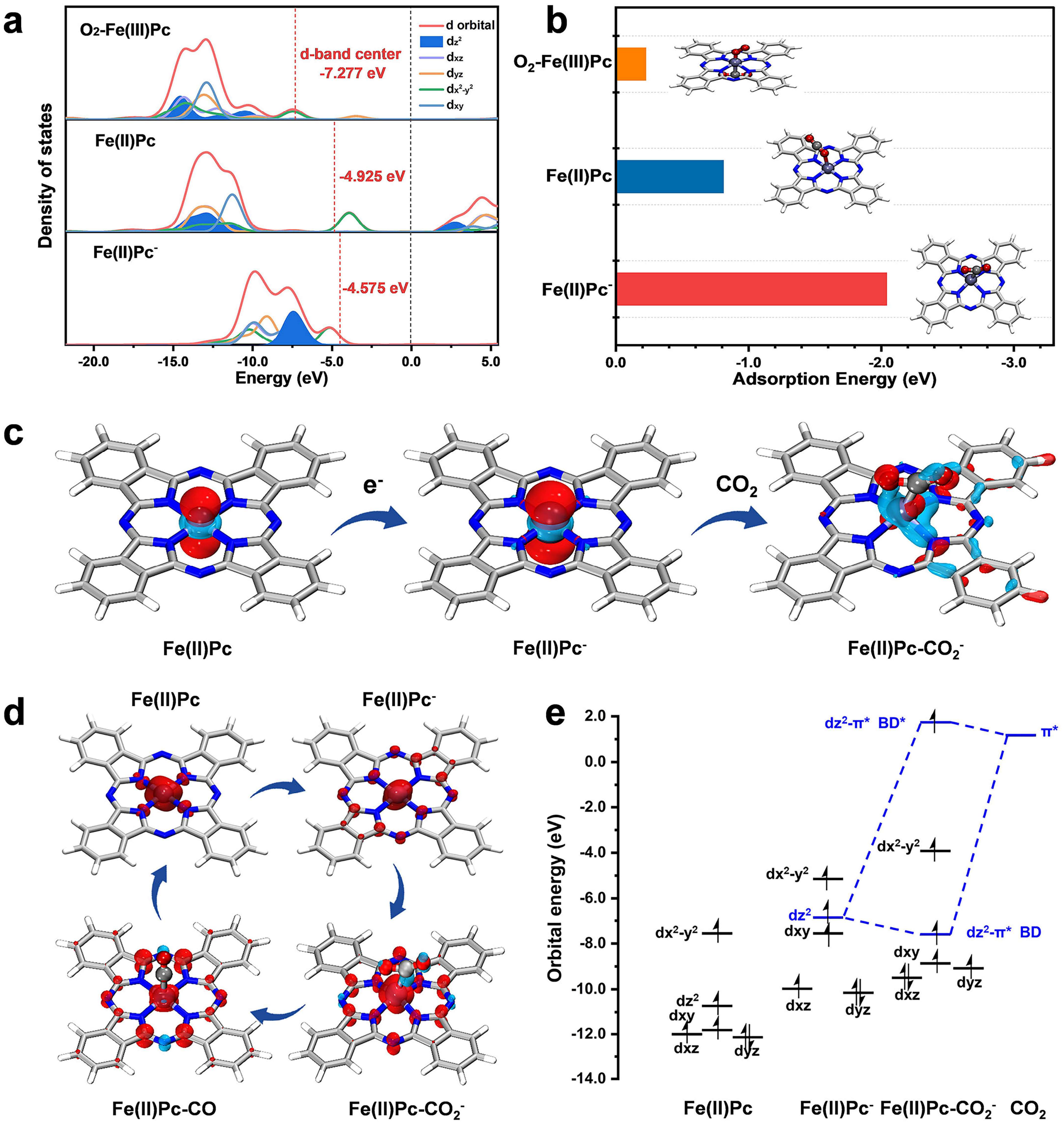

Fig. 6 | Theoretical calculations. a, Density of states (DOS) for Fe-3d orbitals in O_2-Fe(III)Pc, Fe(II)Pc, and Fe(II)Pc$^-$. **b,** The CO_2 adsorption energy over O_2-Fe(III)Pc, Fe(II)Pc, and Fe(II)Pc$^-$. **c,** the dz^2 orbital of Fe(II)Pc and Fe(II)Pc$^-$ and the Kohn–Sham molecular orbital (MO) contours of the dz^2-π^* bonding orbital (BD) of Fe(II)Pc-CO_2^-, where the red and blue regions are positive and negative orbital phases. **d,** The electron spin density plots of Fe(II)Pc, Fe(II)Pc$^-$, Fe(II)Pc-CO_2^- and Fe(II)Pc-CO, the red and blue regions represent α and β electron spin density. **e,** The Kohn–Sham molecular orbital energy-level correlation diagram of Fe(II)Pc, Fe(II)Pc$^-$, and Fe(II)Pc-CO_2^- for the CO_2

activation step.

Conclusions

In summary, with the integration of state-of-the-art *operando* techniques on a model single-Fe-atom catalyst comprising of uniform HS Fe(III) center, we have provided a thorough study of the dynamic structural evolution of single-Fe-atom species under CO_2RR condition. In CO_2-saturated electrolyte, the transformation of O_2-Fe(III)Pc to Fe(II)Pc was observed and the *in-situ* formation of an axial catalytic intermediate of Fe(II)Pc-CO_2^- was evidenced. In contrast, in Ar-saturated electrolyte, the initial HS Fe(III)Pc species started to be irreversibly transformed to metallic iron when the electrochemical potential was decreased to -0.4 V vs. RHE. Meanwhile, the Pc ligand coordinated to single-Fe-atom center experiences a one-electron reduction, in combining with the adsorption and activation of CO_2, that prevent the over-reduction of Fe(II) to Fe(I) species and metallic iron. DFT calculations further reveal that the *in-situ* generated HS Fe(II)Pc$^-$ species with modified d-band center results in a stronger binding with CO_2 molecules, which can effectively boost the CO_2RR. This work provides an in-depth understanding of the electronic structure and dynamic evolution of single-Fe-atom center in CO_2RR and shall shed new light for the future design of high-performance single atom catalysts.

AUTHOR INFORMATION

Corresponding Authors

*frederic.jaouen@umontpellier.fr (F.J.)

*lixn@dicp.ac.cn (X.L.)

*liubin@ntu.edu.sg (B.L.)

Author Contributions

Y.Q.Z., X.N.L., Y.Q.H. and B.L. conceived the project. Y.Q.Z. performed the catalyst synthesis, structural characterization, and CO_2RR performance evaluation. J.Z. conducted the theoretical calculations. Y.Q.Z., S.F.W., Y.R.L., S.B.X., Y.L.T. and X.Y.L. contributed to the XAS spectroscopy measurements and analyses. Y.Q.Z., S.F.W., J.H.W. and X.N.L. carried out the Mössbauer spectroscopy measurements and analyses. Y.Q.Z., S.F.W. and X.Y.R performed the Raman spectroscopy measurements and analyses. Y.Q.Z., X.N.L., B.L. and F.J. wrote and revised the manuscript with inputs from all authors. The project was supervised by X.N.L., Y.Q.H., B.L. and T. Z.

Notes

The authors declare no competing financial interests.

ASSOCIATED CONTENT

Supporting Information

Supplementary data associated with this article is available free of charge via the Internet at www.nature.com/reprints.

Acknowledgements

This work was financially supported by the National Key Research and Development Program of China (No. 2021YFA1500502), the National Natural Science Foundation of China (22102176, U19A2015 and 21925803), CAS Project for Young Scientists in Basic Research (YSBR-051), the Strategic Priority Research Program of the Chinese Academy of Sciences (XDB36030200), Ministry of Education of Singapore (Tier 1: RG4/20 and Tier 2: MOET2EP10120-0002), Agency for Science, Technology and Research (AME IRG: A20E5c0080), and GJTD-2020-08 (K. C. Wong Education Foundation). The XAS data of commercial O_2-Fe(III)Pc and Fe(II)Pc were collected by Jingkun Li at the beamline 8-ID (ISS) of the National Synchrotron Light Source II, a DOE Office of Science User Facility operated for the DOE Office of Science by Brookhaven National Laboratory under contract no. DE-SC0012704. The authors gratefully acknowledge the support of Photon Science Center for Carbon Neutrality.

References

1. Pan, F. *et al.* Boosting CO_2 reduction on Fe-N-C with sulfur incorporation: Synergistic electronic and structural engineering. *Nano Energy* **68**, 104384 (2020).
2. Ju, W. *et al.* Unraveling mechanistic reaction pathways of the electrochemical CO_2 reduction on Fe–N–C single-site catalysts. *ACS Energy Lett.* **4**, 1663-1671 (2019).
3. Lin, L. *et al.* Temperature-dependent CO_2 electroreduction over Fe-N-C and Ni-N-C single-atom catalysts. *Angew. Chem. Int. Ed.* **60**, 26582-26586 (2021).
4. Han, N. *et al.* Supported cobalt polyphthalocyanine for high-performance electrocatalytic CO_2 reduction. *Chem* **3**, 652-664 (2017).
5. Yi, J. D. *et al.* Conductive two-dimensional phthalocyanine-based metal-organic framework nanosheets for efficient electroreduction of CO_2. *Angew. Chem. Int. Ed.* **60**, 17108-17114 (2021).
6. Liu, Y. R. *et al.* Tuning the spin state of the iron center by bridge-bonded Fe-O-Ti ligands for enhanced oxygen reduction. *Angew. Chem. Int. Ed.* **61**, e2021176 (2022).
7. Zhu, Y. S., Zhang, B. S., Liu, X., Wang, D. W. & Su, D. S. Unravelling the structure of electrocatalytically active Fe-N complexes in carbon for the oxygen reduction reaction. *Angew. Chem. Int. Ed.* **53**, 10673-10677 (2014).
8. Qiu, X. F., Zhu, H. L., Huang, J. R., Liao, P. Q. & Chen, X. M. Highly selective CO_2 electroreduction to C_2H_4 using a metal-organic framework with dual active sites. *J. Am. Chem. Soc.* **143**, 7242-7246 (2021).
9. Zhang, M. D. *et al.* Conductive phthalocyanine-based covalent organic framework for highly efficient electroreduction of carbon dioxide. *Small* **16**, 2005254 (2020).

10. Xie, Y. *et al.* High carbon utilization in CO_2 reduction to multi-carbon products in acidic media. *Nat. Catal.* **5**, 564-570 (2022).

11. Yang, H. B. *et al.* Atomically dispersed Ni(I) as the active site for electrochemical CO_2 reduction. *Nat. Energy* **3**, 140-147 (2018).

12. Liu, D., He, Q., Ding, S. & Song, L. Structural regulation and support coupling effect of single-atom catalysts for heterogeneous catalysis. *Adv. Energy Mater.* **10**, 2001482 (2020).

13. Li, X. *et al.* Identification of the electronic and structural dynamics of catalytic centers in single-Fe-atom material. *Chem* **6**, 3440-3454 (2020).

14. Li, J. *et al.* Identification of durable and non-durable FeNx sites in Fe–N–C materials for proton exchange membrane fuel cells. *Nat. Catal.* **4**, 10-19 (2021).

15. Yang, J. *et al.* Dynamic behavior of single-atom catalysts in electrocatalysis: identification of Cu-N3 as an active site for the oxygen reduction reaction. *J. Am. Chem. Soc.* **143**, 14530-14539 (2021).

16. Qiao, B. *et al.* Single-atom catalysis of CO oxidation using Pt_1/FeO_x. *Nat. Chem.* **3**, 634-641 (2011).

17. Jiang, Z. *et al.* Modulating the electronic metal-support interactions in single-atom Pt1-CuO catalyst for boosting acetone oxidation. *Angew. Chem. Int. Ed.* **61**, e202200763 (2022).

18. Deng, Y. *et al.* Few-atom Pt ensembles enable efficient catalytic cyclohexane dehydrogenation for hydrogen production. *J. Am. Chem. Soc.* **144**, 3535-3542 (2022).

19. Xiao, F. *et al.* Atomically dispersed Pt and Fe sites and Pt–Fe nanoparticles for durable proton exchange membrane fuel cells. *Nat. Catal.* **5**, 503-512 (2022).

20. Liu, S. *et al.* Atomically dispersed iron sites with a nitrogen-carbon coating as highly active

and durable oxygen reduction catalysts for fuel cells. *Nat. Energy* **7**, 652-663 (2022).

21. Jin, Z., Li, P., Fang, Z. & Yu, G. Emerging electrochemical techniques for probing site behavior in single-atom electrocatalysts. *Acc. Chem. Res.* **55**, 759-769 (2022).

22. Ahmed, M. I. *et al.* Nitrogenase-inspired atomically dispersed Fe–S–C linkages for improved electrochemical reduction of dinitrogen to ammonia. *ACS Catal.* **12**, 1443-1451 (2022).

23. Huang, H.-C. *et al.* Adsorption energy as a promising single-parameter descriptor for single atom catalysis in the oxygen evolution reaction. *J. Mater. Chem. A* **9**, 6442-6450 (2021).

24. Liu, S. *et al.* Elucidating the electrocatalytic CO_2 reduction reaction over a model single-atom nickel catalyst. *Angew. Chem. Int. Ed.* **59**, 798-803 (2020).

25. Huang, J. *et al.* Modifying redox properties and local bonding of Co_3O_4 by CeO_2 enhances oxygen evolution catalysis in acid. *Nat. Commun.* **12**, 3036 (2021).

26. Chen, J. Y. *et al.* Operando analysis of NiFe and Fe oxyhydroxide electrocatalysts for water oxidation: detection of Fe^{4+} by mossbauer spectroscopy. *J. Am. Chem. Soc.* **137**, 15090-15093 (2015).

27. Gu, J., Hsu, C. S., Bai, L., Chen, H. M. & Hu, X. Atomically dispersed Fe^{3+} sites catalyze efficient CO_2 electroreduction to CO. *Science* **364**, 1091-1094 (2019).

28. Li, J. *et al.* Volcano trend in electrocatalytic CO_2 reduction activity over atomically dispersed metal sites on nitrogen-doped carbon. *ACS Catal.* **9**, 10426-10439 (2019).

29. Li, X. *et al.* Unveiling the in situ generation of a monovalent Fe(I) site in the single-Fe-atom catalyst for electrochemical CO_2 reduction. *ACS Catal.* **11**, 7292-7301 (2021).

30. Ni, L., Theis, P., Paul, S., Stark, R. W. & Kramm, U. I. In situ ^{57}Fe mössbauer study of a porphyrin based FeNC catalyst for ORR. *Electrochim. Acta* **395**, (2021).

31. Primbs, M. *et al.* Establishing reactivity descriptors for platinum group metal (PGM)-free Fe–N–C catalysts for PEM fuel cells. *Energy Environ. Sci.* **13**, 2480-2500 (2020).

32. Jiao, L. *et al.* Chemical vapour deposition of Fe-N-C oxygen reduction catalysts with full utilization of dense Fe-N4 sites. *Nat. Mater.* **20**, 1385-1391 (2021).

33. Lu, Y. *et al.* Identification of the active complex for CO oxidation over single-atom Ir-on-$MgAl_2O_4$ catalysts. *Nat. Catal.* **2**, 149-156 (2018).

34. Ni, L. *et al.* Identification of the catalytically dominant iron environment in iron- and nitrogen-doped carbon catalysts for the oxygen reduction reaction. *J. Am. Chem. Soc.* **144**, 16827–16840 (2022).

35. Kapusta, S. & Hackerman, N. Carbon dioxide reduction at a metal phthalocyanine catalyzed carbon electrode. *J. Electrochem. Soc.* **131** 1511

36. Wang, M., Chen, L., Lau, T. C. & Robert, M. A hybrid co quaterpyridine complex/carbon nanotube catalytic material for CO_2 reduction in water. *Angew. Chem. Int. Ed.* **57**, 7769-7773 (2018).

37. Choi, J. *et al.* Steric modification of a cobalt phthalocyanine/graphene catalyst to give enhanced and stable electrochemical CO_2 reduction to CO. *ACS Energy Lett.* **4**, 666-672 (2019).

38. Li, X. *et al.* Electrocatalytic reduction of CO_2 to CO over iron phthalocyanine-modified graphene nanocomposites. *Carbon* **167**, 658-667 (2020).

39. Manbeck, G. F. & Fujita, E. A review of iron and cobalt porphyrins, phthalocyanines and related complexes for electrochemical and photochemical reduction of carbon dioxide. *J. Porphyr. Phthalocyanines* **19**, 45-64 (2015).

40. Ren, X. *et al.* Electron-withdrawing functional ligand promotes CO_2 reduction catalysis in

single atom catalyst. *Sci. China Chem.* **63**, 1727-1733 (2020).

41. Wang, Q. *et al.* Iron phthalocyanine-graphene donor-acceptor hybrids for visible-light-assisted degradation of phenol in the presence of H_2O_2. *Appl. Catal. B* **192**, 182-192 (2016).

42. Sun, X., Wang, L. & Tan, Z. Improved synthesis of soluble metal-free/metal phthalocyanine tetracarboxylic acids and their application in the catalytic epoxidation of cyclohexene. *Catal. Letters* **145**, 1094-1102 (2015).

43. Seoudi, R., El-Bahy, G. S. & El Sayed, Z. A. FTIR, TGA and DC electrical conductivity studies of phthalocyanine and its complexes. *J. Mol. Struct.* **753**, 119-126 (2005).

44. Baranton, S., Coutanceau, C., Garnier, E. & Léger, J. M. How does α-FePc catalysts dispersed onto high specific surface carbon support work towards oxygen reduction reaction (orr)? *Journal of Electroanalytical Chemistry* **590**, 100-110 (2006).

45. Burtsev, I. D. *et al.* Synthesis and spectral properties of iron(III) tetra- tert -butylphthalocyanine complexes. *Mendeleev Commun.* **27**, 466-469 (2017).

46. Alsudairi, A. *et al.* Resolving the iron phthalocyanine redox transitions for ORR catalysis in aqueous media. *J. Phys. Chem. Lett.* **8**, 2881-2886 (2017).

47. Lu, X. *et al.* Operando elucidation on the working state of immobilized fluorinated iron porphyrin for selective aqueous electroreduction of CO_2 to CO. *ACS Catal.* **11**, 6499-6509 (2021).

48. Gao, L. *et al.* Atomically dispersed iron with densely exposed active sites as bifunctional oxygen catalysts for zinc-air flow batteries. *Small* **18**, e2105892 (2022).

49. Guo, J. *et al.* The synthesis and synergistic catalysis of iron phthalocyanine and its graphene-based axial complex for enhanced oxygen reduction. *Nano Energy* **46**, 347-355 (2018).

50. Filoti, G., Kuz'min, M. D. & Bartolomé, J. Mössbauer study of the hyperfine interactions and spin dynamics inα-iron(II) phthalocyanine. *Phys.Rev.B* **74**, 134420 (2006).

51. Kuzmann, E. *et al.* Mössbauer studies of the interaction of oxygen with solid β-FeII-phthalocyanine. *J. Solid State Chem.* **170**, 118-123 (2003).

52. Lokesh, K. S. & Adriaens, A. Synthesis and characterization of tetra-substituted palladium phthalocyanine complexes. *Dyes Pigm.* **96**, 269-277 (2013).

53. Martin, C. S., Gouveia-Caridade, C., Crespilho, F. N., Constantino, C. J. L. & Brett, C. M. A. Iron phthalocyanine electrodeposited films: characterization and influence on dopamine oxidation. *J. Phys. Chem. C* **120**, 15698-15706 (2016).

54. Alessio, P., Rodriguez-Mendez, M. L., De Saja Saez, J. A. & Constantino, C. J. Iron phthalocyanine in non-aqueous medium forming layer-by-layer films: growth mechanism, molecular architecture and applications. *Phys. Chem. Chem. Phys.* **12**, 3972-3983 (2010).

55. Gunasekara, I. *et al.* Solid phase FePc catalysts for increased stability of oxygen reduction reaction intermediates at the cathode/electrolyte interface in lithium air batteries. *J. Electrochem. Soc.* **164**, A760-A769 (2017).

56. Chen, Z. *et al.* Operando characterization of iron phthalocyanine deactivation during oxygen reduction reaction using electrochemical tip-enhanced raman spectroscopy. *J. Am. Chem. Soc.* **141**, 15684-15692 (2019).

57. Liu, Z., Zhang, X., Zhang, Y. & Jiang, J. Theoretical investigation of the molecular, electronic structures and vibrational spectra of a series of first transition metal phthalocyanines. *Spectrochim.Acta,PartA* **67**, 1232-1246 (2007).